processes

MDPI

Article

Dynamic Modeling and Parameter Identification of Double Casing Joints for Aircraft Fuel Pipelines

Lingxiao Quan [1,2], Chen Fu [1], Renyi Yao [1] and Changhong Guo [1,*]

[1] School of Mechanical Engineering, Yanshan University, Qinhuangdao 066004, China; lingxiao@ysu.edu.cn (L.Q.); 18833549610@163.com (C.F.); 17332973635@163.com (R.Y.)
[2] Hebei Provincial Key Laboratory of Heavy Machinery Fluid Power Transmission and Control, Yanshan University, Qinhuangdao 066004, China
* Correspondence: guochanghong@ysu.edu.cn

Abstract: Double casing joints are flexible pipe joints used for connecting aircraft fuel pipelines, which can compensate for the displacement and corner of the connected pipes and have complex mechanical characteristics. However, it is difficult to use sensors to directly measure the mechanical connection parameters of flexible joints. In this paper, we construct a coupling dynamics model and parameter identification of a double casing joint. Firstly, we analyze the structure and working principle of double-layer casing joints and establish the dynamics model of a single-layer flexible joint based on the transfer matrix method. Then, we deduce the coupling matrix of the inner and outer pipeline according to the deformation coordination conditions combined with matrix dimension extension. We establish the coupling dynamics model of flow–solid coupling of double casing joints. Furthermore, parameters such as equivalent stiffness and damping of each motion of the double casing joint in the casing unit are identified using the force-state mapping (FSM) method, and an analytical solution in the frequency domain under hammering excitation is given by the dynamics model. Finally, the dynamics test bench of the double casing joint for aircraft fuel is set up, and the free mode test of the double casing joint assembly is carried out. The results show that under free boundary hammering excitation, the theoretical and experimental frequency-domain response results are well matched, both obtaining seven main resonance peaks, and the maximum error is 9.45%, which shows the validity of the pipeline dynamics modeling method with a double casing joint.

Keywords: double casing joint; flow–solid coupling; parameters identification; free modal

Citation: Quan, L.; Fu, C.; Yao, R.; Guo, C. Dynamic Modeling and Parameter Identification of Double Casing Joints for Aircraft Fuel Pipelines. *Processes* **2023**, *11*, 2767. https://doi.org/10.3390/pr11092767

Academic Editor: Krzysztof Rogowski

Received: 14 August 2023
Revised: 11 September 2023
Accepted: 13 September 2023
Published: 15 September 2023

1. Introduction

A fuel system is an important airborne system of civil aircraft, and serious accidents may occur when the fuel system is faulty or damaged [1–5]. Therefore, it is of great significance to carry out dynamic analysis of fuel systems for preventing and solving the rupture and leakage problems of fuel pipes. Fuel pipes are installed in sections due to body deformation as well as the need for installation and maintenance. Fuel pipes are installed in sections due to body deformation as well as the need for installation and maintenance. This connection allows a certain degree of axial relative displacement and angular relative change between fuel pipes on both sides of the flexible joint, as to better adapt to the deformation of the airframe and reduce the load generated by the structural deformation of the pipeline [6–8].

Flexible joints are categorized into single-layer and double-layer joints, of which double-layer flexible joints are also known as double casing joints. Generally, single-layer flexible joints are used for the pressure fueling system, water removal system, aeration system, and fuel supply system in the aircraft fuel system. The fuel supply system, which delivers fuel to the engine and the auxiliary power unit of the aircraft, uses double casing joints in order to guarantee its safety [9]. However, this type of connection leads to many

contact problems that need to be considered in the actual analysis process, involving material, geometry, and contact nonlinearities. Especially since double casing joints are tightly combined with small gaps between components, it is extremely difficult to measure connection parameters using sensors. This makes it difficult to accurately analyze the dynamic characteristics of the fuel system. Therefore, it is of great theoretical significance and engineering application value to carry out research on the dynamic modeling and parameter identification of aircraft double casing joints.

In recent years, scholars have carried out a lot of research work on flexible joints. Shi et al. investigated the damage rules of bonding interfaces during flexible joint swinging under a wide temperature range. They proposed a computational method to calculate the sealing reliability of flexible joints. The results show that flexible joints are more prone to failure at high temperatures [10]. Song et al. proposed a parameter identification method for flexible joints combined with offline identification and online compensation. They found that feedforward compensation control can effectively correct model parameters and improve control accuracy [11]. Xu et al. established the special casing of the nipple analysis model using the MARC contact module and simulated the stress of the special thread casing distribution rule and the mechanical properties of the threaded nipple [12]. Vasileios et al. compared the response of continuous pipes and pipes with internal flexible joints under imposed transverse displacement. The experimental results confirmed the very significant contribution of the flexible joints in strain reduction [13]. Konstantino et al. established a mathematical model of an interconnected system and studied the influence of the inherent characteristics of the system, including the flexible joint, on the aircraft power efficiency [14]. Ramezani et al. analyzed the flexible joint of aero-engines using the finite element method and studied the influence of geometric parameters on the performance of flexible joints in detail [15]. While many scholars have carried out research work on flexible joints, there are fewer studies related to the mechanical mechanism, dynamic modeling, and analysis of aircraft double casing joints. As an essential part of the fuel piping system, exploring its dynamic characteristics can contribute to a better iterative design of the fuel system.

Considerable research regarding the fluid–solid coupling dynamics has been reported in the past years. Li et al. proposed a novel fluid–structure coupling modeling and sensing method for a multiphase-free sink vortex-induced vibration mechanism, revealing the vibration evolution mechanism [16,17]. Zhang et al. analyzed the effects of the structural parameters of the pipe on the axial and annular modes of the pipeline and the conversion mechanism of the two modes [18]. Xu et al. used a fourteen-equation model to describe the FSI in a fluid-filled complex pipeline and proposed a generalized solution method for predicting the frequency response of a multi-branch pipeline based on the transfer matrix method [19]. On the foundation of general pipe research, combined with the structural characteristics of the double casing joint, we develop a theoretical analysis of fluid–solid coupling vibration characteristics and summarize its vibration regulation, which is of great significance for predicting the interaction between fluid flow and solid structure.

Force-state mapping (FSM) is a method to identify the equivalent dynamic parameters of a nonlinear connection structure. It considers the nonlinear restoring force generated by the connection structure as a polynomial function of the displacement and velocity of the connection bonding surface. Compared with other methods, this method can establish a complete equation for the force state of the joint surface and can directly represent the stiffness and damping characteristics of the system [20–22]. Hadid et al. used the FSM method to study nonlinear systems with single and multiple degrees of freedom. They proposed a method to obtain an accurate equivalent mass in a nonlinear model using linear fitting and iteration and estimated the sensitivity of the mass or modal mass using excitation frequencies. This led to more accurate identification of the parameters [23]. Kim et al. proposed a method to identify nonlinear connection characteristics from the frequency response function of structural nonlinear connection points. The method utilizes the frequency response of each substructure in the frequency domain and is applicable to

complex structures with nonlinear nodes. The conclusions show that the method has high-accuracy identification [24]. Wang et al. proposed that a nonlinear joint model and dynamic parameters should be recognized simultaneously in practical applications. Therefore, they used the FSM method based on the frequency domain to simultaneously identify the model and dynamic parameters of nonlinear joints [25]. Shu et al. obtained an accurate mathematical model in the blanking stage of a hydraulic fine-blanking press through a least-squares method system identification experiment and proposed a phased PID control strategy. The results show that the new control strategy is very effective in reducing the impact vibration of the hydraulic system [26].

In this paper, a coupling dynamics model is constructed based on the structure and working principle of the double casing joint. Then, the FSM method is adopted to identify the equivalent connection stiffness, damping, and other parameters of the flexible joint in order to solve the numerical solution in the frequency domain under the free boundary. Finally, the validity of the coupling dynamics model and the results of the parameter identification are verified through experiments. The aim of this paper is to lay a theoretical foundation for the accurate modeling of aircraft fuel systems.

2. Working Principle

The double casing joint consists of two parts: the inner joint and the outer joint, as shown in Figure 1. The inner joint is fixed in the form of a clamp, and the outer joint is fixed in the form of a threaded connection and a clip spring. The clamp fixing enables disengaging the pipes in a radial direction, while the clip spring fixing structure disengages the pipes in an axial direction.

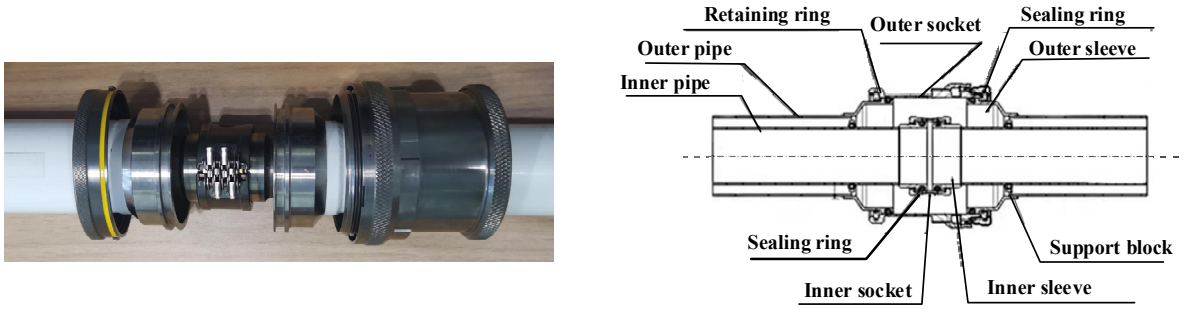

Figure 1. Double casing joint object. (**a**) Object, (**b**) section.

The double casing joint has a dynamic seal formed by the inner and outer sealing rings. In practice, the fuel flows in the inner joint, and there is only air in the outer joint. When the inner seal is damaged, fuel leaks from the inner joint into the outer joint.

When compensating for the displacement and angle of the connected pipe, the working principle of the double casing joint is that the pipe and the sleeve are connected by welding or rotary extrusion forming, which makes the movement between the pipe and the sleeve synchronized. The end of the outer sleeve is equipped with a retaining ring to limit the axial movement of the outer casing, while the end of the inner sleeve has a convex shoulder structure to limit the axial movement of the inner casing. In addition, double casing joints allow both ends of the pipe to twist around the axis. The two layers of the pipe are connected by a support block to ensure the synchronization of the movement of the inner and outer layers of the pipe. However, this synchronization can be lost in the event of plastic deformation of the support block or the pipe itself or in the event of failure of the connection.

3. Theoretical Modeling

3.1. Force Analysis and Dynamic Modeling of Single-Layer Flexible Joints

The force state and working principle of double casing joints are similar to those of single-layer flexible joints. Therefore, the dynamic model of the single-layer flexible joint is established and then extended to the double casing joint. The basic motion of the flexible joint during operation can be divided into translation along the Y-axis, torsion around the Y-axis, deflection around the X-axis, and deflection around the Z-axis. These four motions can be carried out separately or simultaneously.

According to the structure and working principle of the joint, assuming that there is no relative motion between the O-ring and the sealing groove, the sealing ring and pipe sleeve are regarded as a whole. Since rubber material has triple the nonlinear characteristics of material nonlinearity, geometric nonlinearity, and contact nonlinearity, a parallel nonlinear spring-damping element is used to describe this relationship. The dynamic model of the flexible joint is shown in Figure 2.

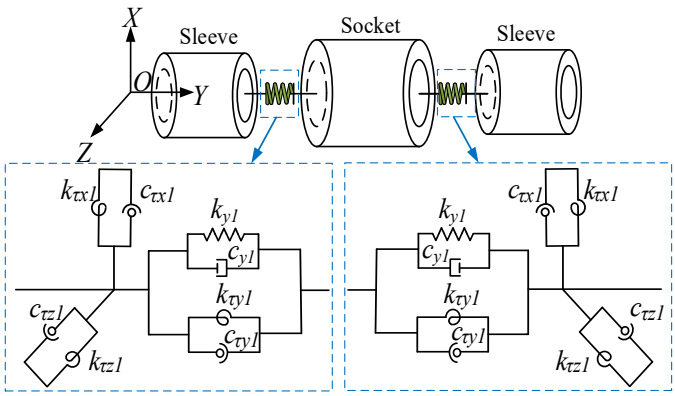

Figure 2. Dynamic modeling of flexible joint.

In Figure 2, the convex shoulder of the sleeve and the variable diameter transition structure from the sleeve to the pipeline, as well as the fixing and limiting mechanism outside the socket, are neglected. The sleeve and socket are equivalent to straight pipe units, and the straight pipe units are connected by four sets of parallel nonlinear spring-damping units, which are designated as connection units. There are two connection units in the dynamic model of the flexible joint, and the stiffness and damping parameters contained in the two connection units are the same. The dynamic characteristics can be solved using the method of fluid–solid coupling equation and transfer matrix.

In this paper, the fourteen-equation model is used to establish the dynamic model of the double casing joint. The pipe forces are mainly composed of inertial force, axial internal and external force on the pipe wall, friction between the pipe wall and fluid, fluid pressure, and gravity. Fourteen system variables in the fourteen-equation model can be written as a state vector [27]:

$$\boldsymbol{\eta}(z,t) = \left[V\ \mathrm{P}\ \dot{\omega}_z\ f_z\ \mathrm{M}_y\ \dot{\theta}_y\ \dot{\omega}_x\ f_x\ \mathrm{M}_x\ \dot{\theta}_x\ \dot{\omega}_y\ f_y\ \dot{\theta}_z\ \mathrm{M}_z\right]^T \tag{1}$$

where V represents the fluid velocity; P represents the fluid pressure; $\dot{\omega}$ represents the pipe velocity; f represents the forces in the cross-section; M represents the moment; x, y, and z are the directional subscripts; θ represents the deflection angle of pipe; $\dot{\theta}$ represents the angular velocity of pipe wall; and m_0 represents plug mass.

The matrix expression of the fluid–solid coupling fourteen-equation model of the pipe can be written as follows:

$$\mathbf{A}\frac{\partial \boldsymbol{\eta}(z,t)}{\partial t} + \mathbf{B}\frac{\partial \boldsymbol{\eta}(z,t)}{\partial z} + \mathbf{C}\boldsymbol{\eta}(z,t) + \mathbf{D} = \mathbf{y}(z,t) \tag{2}$$

Here, **A**, **B**, and **C** are coefficient matrices within the dimensional scales, multiplied by **A** and **B**, which are the constant terms of time and space differentiation, respectively. **C** and **D** are coefficient matrices, including friction and viscous damping and gravity, respectively. Vector y describes the external excitation.

$\tilde{\eta}(z,s) = \int_0^\infty e^{-st}\eta(z,t)dt$, $\tilde{y}(z,s) = \int_0^\infty e^{-st}y(z,t)dt$. The Laplace transform of Equation (2) can be simplified to give the frequency-domain differential equation:

$$\tilde{\boldsymbol{\eta}}(z,s) + \mathbf{A}^{*-1}\mathbf{B}\frac{\partial\tilde{\boldsymbol{\eta}}(z,s)}{\partial z} = \mathbf{A}^{*-1}\mathbf{y}^*(z,s) \tag{3}$$

where $\mathbf{A}^* = s\mathbf{A} + \mathbf{C}$, $y^*(z,s) = \tilde{y}(z,s) - \frac{1}{s}\mathbf{D} - \mathbf{A}\eta(z,t)|_{t=0}$.

Given that the eigenvalue of $\mathbf{A}^{*-1}\mathbf{B}$ is $\mathbf{T}$ and the eigenvector matrix is $\mathbf{V}$, $\mathbf{V}^{-1}\mathbf{A}^{*-1}\mathbf{B}\mathbf{V} = \mathbf{T}$, $\mathbf{T}$ and $\mathbf{V}$ can be written as:

$$\mathbf{T} = \begin{pmatrix} \lambda_1(s) & & & \\ & \lambda_2(s) & & \\ & & \ddots & \\ & & & \lambda_{14}(s) \end{pmatrix} \tag{4}$$

$$V = \begin{bmatrix} \xi_1(s) & \xi_2(s) & \cdots & \xi_{14}(s) \end{bmatrix}^T \tag{5}$$

where eigenvectors, $\xi_i(s)$, and eigenvalues, $\lambda_i(s)$, correspond to each other.

Given that $\tilde{\boldsymbol{\Phi}}(z,s) = \mathbf{V}^{-1}\tilde{\eta}(z,s)$, $\tilde{\boldsymbol{\Phi}}_r(z,s) = \mathbf{V}^{-1}\mathbf{A}^{-1}y^*(z,s)$, Equation (3) can be expressed as:

$$\frac{\partial\tilde{\boldsymbol{\Phi}}(z,s)}{\partial z} + \mathbf{T}^{-1}\tilde{\boldsymbol{\Phi}}(z,s) = \mathbf{T}^{-1}\tilde{\boldsymbol{\Phi}}_r(z,s) \tag{6}$$

The linear ordinary differential Equation (6) can be solved as:

$$\tilde{\boldsymbol{\Phi}}(z,s) = \mathbf{E}(z,s)\tilde{\boldsymbol{\Phi}}_0(s) + \tilde{\boldsymbol{\Phi}}_r^*(z,s) \tag{7}$$

where

$$\begin{cases} \mathbf{E}(z,s) = diag\{e(-sz/\lambda_1(s)), e(-sz/\lambda_2(s)), \cdots e(-sz/\lambda_{14}(s))\} \\ \tilde{\boldsymbol{\Phi}}_r^*(z,s) = \begin{pmatrix} \tilde{\boldsymbol{\Phi}}_1(z,s) & \tilde{\boldsymbol{\Phi}}_2(z,s) & \cdots & \tilde{\boldsymbol{\Phi}}_{14}(z,s) \end{pmatrix} \\ \tilde{\boldsymbol{\Phi}}_i(z,s) = \frac{se^{-sz/\lambda_i(s)}}{\lambda_i(s)}\int_0^z \tilde{\boldsymbol{\Phi}}_{ri}(x,s)e^{sx/\lambda_i(s)}dx = \tilde{\boldsymbol{\Phi}}_{ri}(z,s)\left(1 - e^{sx/\lambda_i(s)}\right), (1 \le i \le 14) \end{cases} \tag{8}$$

Substituting $\tilde{\boldsymbol{\Phi}}(z,s) = \mathbf{V}^{-1}\tilde{\eta}(z,s)$ into Equation (7) provides

$$\tilde{\eta}(z,s) = \mathbf{V}\mathbf{E}(z,s)\tilde{\boldsymbol{\Phi}}_0(s) + \mathbf{V}\tilde{\boldsymbol{\Phi}}_r^*(z,s) \tag{9}$$

For the piping system, the form of excitation is basically centralized, and there is no spatially distributed excitation. Substituting $z = 0$, $\mathbf{E}(0,s) = \mathbf{I}_{14\times14}$ and $\tilde{\boldsymbol{\Phi}}_r(z,s) = 0_{14\times1}$ into Equation (9) provides:

$$\tilde{\boldsymbol{\Phi}}_0(s) = \mathbf{V}^{-1}\tilde{\eta}(0,s) \tag{10}$$

Substituting Equation (10) into (9) obtains the solution of the pipeline fluid–solid coupling fourteen-equation model in the Rasch domain as follows:

$$\tilde{\eta}(z,s) = \mathbf{V}\mathbf{E}(z,s)\mathbf{V}^{-1}\tilde{\eta}(0,s) \tag{11}$$

Define the transfer matrix of the pipeline field as:

$$\mathbf{U}(z,s) = \mathbf{V}\mathbf{E}(z,s)\mathbf{V}^{-1} \tag{12}$$

The frequency-domain solution of the pipeline fluid–solid coupling fourteen-equation model expressed in terms of the transfer matrix can be written as:

$$\tilde{\eta}(z,s) = \mathbf{U}(z,s)\tilde{\eta}(0,s) \tag{13}$$

For a pipe of length L, the boundary conditions at both ends of the pipeline satisfy the following relationship:

$$\begin{cases} [\mathbf{D}_0(s)]_{7\times14}[\tilde{\eta}_{0s}]_{14\times1} = [\mathbf{Q}_0(s)]_{7\times1} \\ [\mathbf{D}_L(s)]_{7\times14}[\tilde{\eta}_{Ls}]_{14\times1} = [\mathbf{Q}_L(s)]_{7\times1} \end{cases} \tag{14}$$

where $\mathbf{D}_0(s)$ and $\mathbf{D}_L(s)$ are the constraint state matrix at the beginning and end of the pipe, and $\mathbf{Q}_0(s)$ and $\mathbf{Q}_L(s)$ are the excitation matrix at the beginning and the end of the pipe.

The relation of the two state vectors of the single-pipe section can be expressed as:

$$\tilde{\eta}(L,s) = \mathbf{U}(L,s)\tilde{\eta}(0,s) \tag{15}$$

Assuming that the total length of the pipe is L and that the pipe has n simple sections consisting of pipe units, the overall transfer matrix of the pipe system is as follows:

$$\mathbf{U}_{\text{all}}(s) = \mathbf{U}_N(L_N,s)\cdots\mathbf{U}_i(L_i,s)\cdots\mathbf{U}_1(L_1,s) \tag{16}$$

where $\mathbf{U}_i$ is the transfer matrix of each pipe unit, and L_i is the length of each pipe unit.

Then, the state variables at the beginning of the series pipe system can be represented by the constrained state matrix and the excitation matrix as:

$$\tilde{\eta}_1(0,s) = \mathbf{D}^{*-1}(s)\mathbf{Q}(s) \tag{17}$$

where

$$\mathbf{D}^*(s) = \begin{pmatrix} \mathbf{D}_0(s) \\ \mathbf{D}_L(s)\mathbf{U}_{\text{all}}(s) \end{pmatrix},\ \mathbf{Q}(s) = \begin{pmatrix} \mathbf{Q}_0(s) \\ \mathbf{Q}_L(s) \end{pmatrix} \tag{18}$$

Similarly, the state variables, $\tilde{\eta}(z,s)$, at any position of the piping system can be obtained from the initial state variables, $\tilde{\eta}_1(0,s)$, and the overall transfer matrix of the piping system.

3.2. Dynamical Model of Double Casing Joint

According to Figure 2, the fluid–solid coupling dynamic model of the inner and outer joint is established respectively. Then, the metal support block is equivalent to a coupling spring unit, which can further obtain the dynamic model of the double casing joint, as shown in Figure 3.

In Figure 3, the dynamic model of the double casing joint is divided into eighteen cross-sections, of which the first section is the beginning and the eighteenth section is the end. The region between the first and second sections is designated as uncoupled region 1–2, where there is no connection between the inner and outer layers in the uncoupled zone. There is no connection between the inner and outer layers in the uncoupled regions. The region between the third cross-section and the fourth cross-section is designated as coupling region 3–4. The inner and outer layers of the coupling region are connected by the support blocks, and the connection relationship can be equated to six sets of spring damping. There is also coupling region 15–16 in a similar condition. The uncoupled zones 5–6 and 13–14 contain outer joint connection units. The uncoupled zones 8–9 and 10–11 contain inner joint connection units. The form of the inner and outer joint connection units is the same as that of the single-layer flexible joint connection unit.

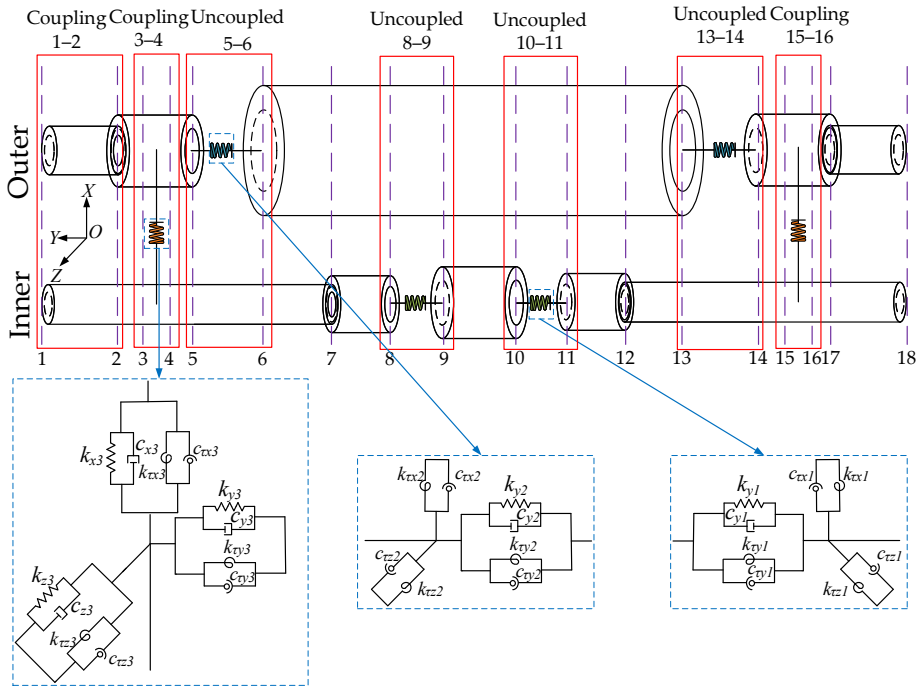

Figure 3. Dynamic modeling of double casing joint.

For the parallel form of the model, a new transfer matrix can be established by the principle of logical structure alignment with matrix dimension extension to realize the structural coupling of the parallel piping system.

In deriving the transfer matrix of double casing joint, it is stipulated that the corner mark "I" indicates the outer layer, the corner mark "II" indicates the inner layer, and the corner mark "III" indicates the support block. By taking coupling area 3–4 as an example, according to the deformation coordination condition and the relationship between force (moment) and displacement (angle), the coordination equation of coupling area 3–4 on the outer pipe is deduced as:

$$\begin{Bmatrix} V_{\mathrm{I}}^{L} = V_{\mathrm{I}}^{R} & \dot{u}_{z\mathrm{I}}^{L} = \dot{u}_{z\mathrm{I}}^{R} \\ P_{\mathrm{I}}^{L} = P_{\mathrm{I}}^{R} & f_{z\mathrm{I}}^{L} = f_{z\mathrm{I}}^{R} + \left(\frac{k_{z3}}{s} + c_{z3}\right)\left(\dot{u}_{z\mathrm{I}}^{R} - \dot{u}_{z\mathrm{II}}^{R}\right) \\ \dot{u}_{y\mathrm{I}}^{L} = \dot{u}_{y\mathrm{I}}^{R} & \dot{\theta}_{x\mathrm{I}}^{L} = \dot{\theta}_{x\mathrm{I}}^{R} \\ f_{y\mathrm{I}}^{L} = f_{y\mathrm{I}}^{R} + \left(\frac{k_{y3}}{s} + c_{y3}\right)\left(\dot{u}_{y\mathrm{I}}^{R} - \dot{u}_{y\mathrm{II}}^{R}\right) & M_{x\mathrm{I}}^{L} = M_{x\mathrm{I}}^{R} + \left(\frac{k_{\tau x3}}{s} + c_{\tau x3}\right)\left(\dot{\theta}_{x\mathrm{I}}^{R} - \dot{\theta}_{x\mathrm{II}}^{R}\right) \\ \dot{u}_{x\mathrm{I}}^{L} = \dot{u}_{x\mathrm{I}}^{R} & \dot{\theta}_{y\mathrm{I}}^{L} = \dot{\theta}_{y\mathrm{I}}^{R} \\ f_{x\mathrm{I}}^{L} = f_{x\mathrm{I}}^{R} + \left(\frac{k_{x3}}{s} + c_{x3}\right)\left(\dot{u}_{x\mathrm{I}}^{R} - \dot{u}_{x\mathrm{II}}^{R}\right) & M_{y\mathrm{I}}^{L} = M_{y\mathrm{I}}^{R} + \left(\frac{k_{\tau y3}}{s} + c_{\tau y3}\right)\left(\dot{\theta}_{y\mathrm{I}}^{R} - \dot{\theta}_{y\mathrm{II}}^{R}\right) \\ \dot{\theta}_{z\mathrm{I}}^{L} = \dot{\theta}_{z\mathrm{I}}^{R} & M_{z\mathrm{I}}^{L} = M_{z\mathrm{I}}^{R} + \left(\frac{k_{\tau z3}}{s} + c_{\tau z3}\right)\left(\dot{\theta}_{z\mathrm{I}}^{R} - \dot{\theta}_{z\mathrm{II}}^{R}\right) \end{Bmatrix} \quad (19)$$

Similarly, the coordination equation on the inner pipeline can be obtained as:

$$\begin{Bmatrix} V_{\mathrm{II}}^{L} = V_{\mathrm{II}}^{R} & \dot{u}_{z\mathrm{II}}^{L} = \dot{u}_{z\mathrm{II}}^{R} \\ P_{\mathrm{II}}^{L} = P_{\mathrm{II}}^{R} & f_{z\mathrm{II}}^{L} = f_{z\mathrm{II}}^{R} + \left(\frac{k_{z3}}{s} + c_{z3}\right)\left(\dot{u}_{z\mathrm{II}}^{R} - \dot{u}_{z\mathrm{I}}^{R}\right) \\ \dot{u}_{y\mathrm{II}}^{L} = \dot{u}_{y\mathrm{II}}^{R} & \dot{\theta}_{x\mathrm{II}}^{L} = \dot{\theta}_{x\mathrm{II}}^{R} \\ f_{y\mathrm{II}}^{L} = f_{y\mathrm{II}}^{R} + \left(\frac{k_{y3}}{s} + c_{y3}\right)\left(\dot{u}_{y\mathrm{II}}^{R} - \dot{u}_{y\mathrm{I}}^{R}\right) & M_{x\mathrm{II}}^{L} = M_{x\mathrm{II}}^{R} + \left(\frac{k_{\tau x3}}{s} + c_{\tau x3}\right)\left(\dot{\theta}_{x\mathrm{II}}^{R} - \dot{\theta}_{x\mathrm{I}}^{R}\right) \\ \dot{u}_{x\mathrm{II}}^{L} = \dot{u}_{x\mathrm{II}}^{R} & \dot{\theta}_{y\mathrm{II}}^{L} = \dot{\theta}_{y\mathrm{II}}^{R} \\ f_{x\mathrm{II}}^{L} = f_{x\mathrm{II}}^{R} + \left(\frac{k_{x3}}{s} + c_{x3}\right)\left(\dot{u}_{x2}^{R} - \dot{u}_{x1}^{R}\right) & M_{y\mathrm{II}}^{L} = M_{y\mathrm{II}}^{R} + \left(\frac{k_{\tau y3}}{s} + c_{\tau z3}\right)\left(\dot{\theta}_{y\mathrm{II}}^{R} - \dot{\theta}_{y\mathrm{I}}^{R}\right) \\ \dot{\theta}_{z\mathrm{II}}^{L} = \dot{\theta}_{z\mathrm{II}}^{R} & M_{z\mathrm{II}}^{L} = M_{z\mathrm{III}}^{R} + \left(\frac{k_{\tau z3}}{s} + c_{\tau z3}\right)\left(\dot{\theta}_{z\mathrm{II}}^{R} - \dot{\theta}_{z\mathrm{I}}^{R}\right) \end{Bmatrix} \tag{20}$$

The subscripts "*R*" and "*L*" indicate the right and left ends of the coupling region, respectively. The transfer matrix of the coupling region between the two regions is:

$$\left[V_{\mathrm{I}}\ P_{\mathrm{I}}\ \dot{u}_{z\mathrm{I}}\ \cdots\ M_{z\mathrm{I}}\ V_{\mathrm{II}}\ P_{\mathrm{II}}\ \dot{u}_{z\mathrm{II}}\ \cdots\ M_{z\mathrm{II}}\right]_{L}^{\mathrm{T}} = N_{\mathrm{III}}\left[V_{\mathrm{I}}\ P_{\mathrm{I}}\ \dot{u}_{z\mathrm{I}}\ \cdots\ M_{z\mathrm{I}}\ V_{\mathrm{II}}\ P_{\mathrm{II}}\ \dot{u}_{z\mathrm{II}}\ \cdots\ M_{z\mathrm{II}}\right]_{R}^{\mathrm{T}} \tag{21}$$

where

$$N_{\mathrm{III}} = \begin{bmatrix} \tilde{N}_{14\times14} & \widehat{N}_{14\times14} \\ \widehat{N}_{14\times14} & \tilde{N}_{14\times14} \end{bmatrix} \tag{22}$$

$$\tilde{N}_{14\times14} = \begin{bmatrix} 1 & 0 & 0 & 0 & 0 & 0 & 0 & 0 & 0 & 0 & 0 & 0 & 0 & 0 \\ 0 & 1 & 0 & 0 & 0 & 0 & 0 & 0 & 0 & 0 & 0 & 0 & 0 & 0 \\ 0 & 0 & 1 & 0 & 0 & 0 & 0 & 0 & 0 & 0 & 0 & 0 & 0 & 0 \\ 0 & 0 & \frac{k_{z3}}{s} + c_{z3} & 1 & 0 & 0 & 0 & 0 & 0 & 0 & 0 & 0 & 0 & 0 \\ 0 & 0 & 0 & 0 & 1 & 0 & 0 & 0 & 0 & 0 & 0 & 0 & 0 & 0 \\ 0 & 0 & 0 & 0 & 0 & 1 & 0 & 0 & 0 & 0 & 0 & 0 & 0 & 0 \\ 0 & 0 & 0 & 0 & 0 & \frac{k_{\tau y3}}{s} + c_{\tau y3} & 1 & 0 & 0 & 0 & 0 & 0 & 0 & 0 \\ 0 & 0 & 0 & 0 & 0 & 0 & \frac{k_{x3}}{s} + c_{x3} & 1 & 0 & 0 & 0 & 0 & 0 & 0 \\ 0 & 0 & 0 & 0 & 0 & 0 & 0 & 0 & 1 & 0 & 0 & 0 & 0 & 0 \\ 0 & 0 & 0 & 0 & 0 & 0 & 0 & 0 & 0 & 1 & 0 & 0 & 0 & 0 \\ 0 & 0 & 0 & 0 & 0 & 0 & 0 & 0 & 0 & \frac{k_{\tau x3}}{s} + c_{\tau x3} & 1 & 0 & 0 & 0 \\ 0 & 0 & 0 & 0 & 0 & 0 & 0 & 0 & 0 & 0 & \frac{k_{y3}}{s} + c_{y3} & 1 & 0 & 0 \\ 0 & 0 & 0 & 0 & 0 & 0 & 0 & 0 & 0 & 0 & 0 & 0 & 1 & 0 \\ 0 & 0 & 0 & 0 & 0 & 0 & 0 & 0 & 0 & 0 & 0 & 0 & \frac{k_{\tau z3}}{s} + c_{\tau z3} & 1 \end{bmatrix} \tag{23}$$

$$\widehat{N}_{14\times14} = \begin{bmatrix} 1 & 0 & 0 & 0 & 0 & 0 & 0 & 0 & 0 & 0 & 0 & 0 & 0 & 0 \\ 0 & 1 & 0 & 0 & 0 & 0 & 0 & 0 & 0 & 0 & 0 & 0 & 0 & 0 \\ 0 & 0 & 1 & 0 & 0 & 0 & 0 & 0 & 0 & 0 & 0 & 0 & 0 & 0 \\ 0 & 0 & -\frac{k_{z3}}{s} - c_{z3} & 1 & 0 & 0 & 0 & 0 & 0 & 0 & 0 & 0 & 0 & 0 \\ 0 & 0 & 0 & 0 & 1 & 0 & 0 & 0 & 0 & 0 & 0 & 0 & 0 & 0 \\ 0 & 0 & 0 & 0 & 0 & 1 & 0 & 0 & 0 & 0 & 0 & 0 & 0 & 0 \\ 0 & 0 & 0 & 0 & 0 & -\frac{k_{\tau y3}}{s} - c_{\tau y3} & 1 & 0 & 0 & 0 & 0 & 0 & 0 & 0 \\ 0 & 0 & 0 & 0 & 0 & 0 & -\frac{k_{x3}}{s} - c_{x3} & 1 & 0 & 0 & 0 & 0 & 0 & 0 \\ 0 & 0 & 0 & 0 & 0 & 0 & 0 & 0 & 1 & 0 & 0 & 0 & 0 & 0 \\ 0 & 0 & 0 & 0 & 0 & 0 & 0 & 0 & 0 & 1 & 0 & 0 & 0 & 0 \\ 0 & 0 & 0 & 0 & 0 & 0 & 0 & 0 & 0 & -\frac{k_{\tau x3}}{s} - c_{\tau x3} & 1 & 0 & 0 & 0 \\ 0 & 0 & 0 & 0 & 0 & 0 & 0 & 0 & 0 & 0 & -\frac{k_{y3}}{s} - c_{y3} & 1 & 0 & 0 \\ 0 & 0 & 0 & 0 & 0 & 0 & 0 & 0 & 0 & 0 & 0 & 0 & 1 & 0 \\ 0 & 0 & 0 & 0 & 0 & 0 & 0 & 0 & 0 & 0 & 0 & 0 & -\frac{k_{\tau z3}}{s} - c_{\tau z3} & 1 \end{bmatrix} \tag{24}$$

In uncoupled region 1–2, the transfer relation between the two pipe sections is satisfied:

$$\begin{cases} \eta_{L1}^{\mathrm{I}} = U_1^{\mathrm{I}} \eta_{R1}^{\mathrm{I}} \\ \eta_{L1}^{\mathrm{II}} = U_1^{\mathrm{II}} \eta_{R1}^{\mathrm{II}} \end{cases} \tag{25}$$

The further matrix form can be written as:

$$\begin{bmatrix} \eta_{L1}^{\mathrm{I}} \\ \eta_{L1}^{\mathrm{II}} \end{bmatrix} = \begin{bmatrix} U_1^{\mathrm{I}} & 0 \\ 0 & U_1^{\mathrm{II}} \end{bmatrix} \begin{bmatrix} \eta_{R1}^{\mathrm{I}} \\ \eta_{R1}^{\mathrm{II}} \end{bmatrix} \tag{26}$$

In coupling region 3–4, the transfer relation is satisfied:

$$\begin{bmatrix} \eta_{R2}^{\mathrm{I}} \\ \eta_{R2}^{\mathrm{II}} \end{bmatrix} = N_{\mathrm{III}} \begin{bmatrix} \eta_{R3}^{\mathrm{I}} \\ \eta_{R3}^{\mathrm{II}} \end{bmatrix} \tag{27}$$

Similarly, the coupled and uncoupled regions transfer relations are constructed in the same way. Then, the total transfer matrix can be written as:

$$\begin{bmatrix} \phi_{L1}^{\mathrm{I}} \\ \phi_{L1}^{\mathrm{II}} \end{bmatrix} = H \begin{bmatrix} \phi_{R18}^{\mathrm{I}} \\ \phi_{R18}^{\mathrm{II}} \end{bmatrix} \tag{28}$$

where

$$H = \begin{bmatrix} U_1^{\mathrm{I}} & 0 \\ 0 & U_1^{\mathrm{II}} \end{bmatrix} \begin{bmatrix} U_2^{\mathrm{I}} & 0 \\ 0 & U_2^{\mathrm{II}} \end{bmatrix} N_{\mathrm{III}} \begin{bmatrix} U_4^{\mathrm{I}} & 0 \\ 0 & U_4^{\mathrm{II}} \end{bmatrix} \begin{bmatrix} N_{\mathrm{I}} & 0 \\ 0 & \mathrm{I} \end{bmatrix} \begin{bmatrix} U_6^{\mathrm{I}} & 0 \\ 0 & U_6^{\mathrm{II}} \end{bmatrix} \begin{bmatrix} U_7^{\mathrm{I}} & 0 \\ 0 & U_7^{\mathrm{II}} \end{bmatrix} \begin{bmatrix} \mathrm{I} & 0 \\ 0 & N_{\mathrm{II}} \end{bmatrix} \begin{bmatrix} U_9^{\mathrm{I}} & 0 \\ 0 & U_9^{\mathrm{II}} \end{bmatrix} \begin{bmatrix} \mathrm{I} & 0 \\ 0 & N_{\mathrm{II}} \end{bmatrix} \begin{bmatrix} U_{11}^{\mathrm{I}} & 0 \\ 0 & U_{11}^{\mathrm{II}} \end{bmatrix} \begin{bmatrix} U_{12}^{\mathrm{I}} & 0 \\ 0 & U_{12}^{\mathrm{II}} \end{bmatrix} \begin{bmatrix} N_{\mathrm{I}} & 0 \\ 0 & \mathrm{I} \end{bmatrix} \begin{bmatrix} U_{14}^{\mathrm{I}} & 0 \\ 0 & U_{14}^{\mathrm{II}} \end{bmatrix} N_{\mathrm{III}} \begin{bmatrix} U_{16}^{\mathrm{I}} & 0 \\ 0 & U_{16}^{\mathrm{II}} \end{bmatrix} \begin{bmatrix} U_{17}^{\mathrm{I}} & 0 \\ 0 & U_{17}^{\mathrm{II}} \end{bmatrix} \tag{29}$$

In the solution, the method of introducing boundary conditions corresponding to each state vector is the same as that before matrix dimensioning. It also conforms to the principle of logical alignment so the constraint and excitation matrices of the double casing joint can be expressed as:

$$\mathbf{D}^*(s) = \begin{pmatrix} \mathbf{D}_0^{\mathrm{I}}(s) & \mathbf{0}_{14\times14} \\ \mathbf{D}_L^{\mathrm{I}}(s)H & \\ & \mathbf{D}_0^{\mathrm{II}}(s) \\ \mathbf{0}_{14\times14} & \mathbf{D}_L^{\mathrm{II}}(s)H \end{pmatrix}_{28\times28} \tag{30}$$

$$\mathbf{Q}(s) = \begin{pmatrix} \mathbf{Q}_0^{\mathrm{I}}(s) \\ \mathbf{Q}_L^{\mathrm{I}}(s) \\ \mathbf{Q}_0^{\mathrm{II}}(s) \\ \mathbf{Q}_L^{\mathrm{II}}(s) \end{pmatrix} \tag{31}$$

Equation (28) is the transfer matrix model of the double casing joint. In the flow–solid coupling analysis of the pipeline containing a double casing joint, if the transfer matrix equation of the pipeline system needs to be constructed, the transfer matrix model of the double casing joint can be added to the corresponding part of the joint.

4. Parameter Identification

4.1. Principle of FSM Method

The double casing joints are tightly combined with small gaps between components, making it very difficult to directly measure connection parameters such as casing joint stiffness and damping by using sensors. Secondly, the casing joint dynamics model cannot be solved without accurate connection parameters. Consequently, this makes it difficult to accurately analyze the dynamic characteristics of the aircraft fuel pipelines. Therefore, this paper combines the numerical simulation method and the force-state mapping (FSM) method to identify the equivalent connection parameters, such as stiffness and damping. The double casing is a nonlinear system, and C and K are not only related to x but also related to $\dot{x}$; they are functions of x and $\dot{x}$, and the equation of motion can be expressed as:

$$M\ddot{x} + C(x, \dot{x})\dot{x} + K(x, \dot{x})x = F(t) \tag{32}$$

where M is the system mass matrix, C is the damping matrix, K is the stiffness matrix, $\ddot{x}$ is the acceleration, $\dot{x}$ is the velocity, x is the displacement, and $F(t)$ is the excitation force.

Variation in Equation (1) obtains the equation of motion of the nonlinear system as:

$$f(x,\dot{x}) = C(x,\dot{x})\dot{x} + K(x,\dot{x})x = F(t) - M\ddot{x} \tag{33}$$

where $f(x,\dot{x})$ is the restoring force generated by the nonlinear system.

The stiffness and damping are not constant. Thus, after obtaining the cross-section scatter diagram when the velocity and displacement are 0, the data are fitted. The sinusoidal load in the harmonic load is selected for the excitation force (torque):

$$\begin{aligned} F(t) &= F\sin(2\pi ft) \\ T(t) &= T\sin(2\pi ft) \end{aligned} \tag{34}$$

where F is the amplitude of the excitation force, T is the amplitude of the excitation torque, and f is the frequency of the excitation force (torque).

The excitation frequency should be far from the resonance frequency [28,29]. The parameter identification of the double casing joint connection structure is divided into three steps. Firstly, the constrained modal analysis with pre-stress is carried out for the inner and outer joints, and the sleeve is fixedly supported in order to determine the frequency and amplitude of the sinusoidal excitation force. Secondly, by applying the excitation to obtain the FSM scatter diagram, the inner and outer joint models are fixed at one end and a sinusoidal excitation force (moment) is applied at the other end; the moment is applied at the position of the coupling point RP at the end surface of the pipe. Thirdly, MATLAB is used for data interpolation and fitting.

In order to reduce the influence of brackets, clamps, and pipes on the identification of the joint connection parameters, the clamp, bolt nut, and bracket are removed from the double casing finite element model. The pipes connected to the joint are shortened to a position 10 cm from the outer joint sleeve. In addition, the internal constraints of the joint remain unchanged. The friction coefficient between the O-ring and the metal parts is taken as 0.6. A schematic of the model used to identify the parameters of the inner and outer joint is shown in Figure 4, including critical components, such as the sleeve, socket, and pipe.

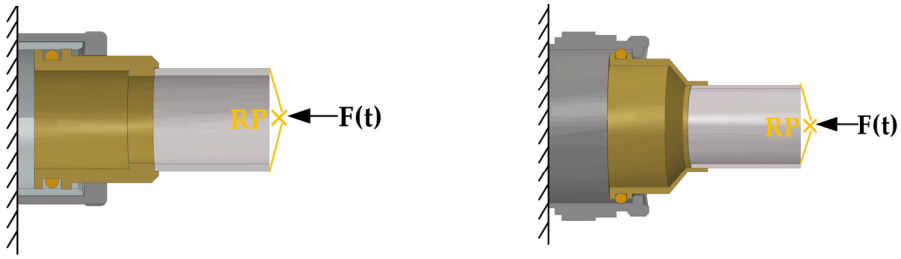

Figure 4. Schematic of the model. (**a**) Inner joint. (**b**) Outer joint.

In order to avoid system resonance when the excitation force (torque) is applied, the sleeve is given a fixed constraint; then, the constrained modal analysis with pre-stress is carried out for the inner and outer joints. The crucial components of the inner joint, such as the socket and pipe, are meshed by the sweep method, the sleeve is meshed by the structured mesh method, and the element type mainly adopts an eight-node linear hexahedron element, a reduction integral, and sand control C3D8R. The sealing ring is a super-elastic material, and the unit type is chosen to be simulated using a hybrid formulation, which can simulate the completely incompressible characteristics. The mesh generation of the inner joint is shown in Figure 5.

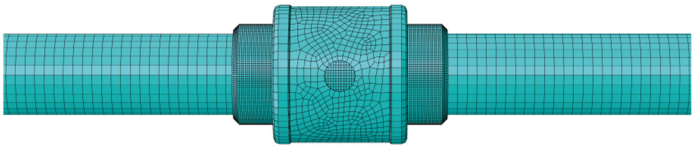

Figure 5. Mesh generation method of inner joint.

When the inner and outer joints are stressed, the seal ring will be in compression and their pre-stress will have a large impact on the modal analysis. Also, the sealing performance is important for the safety of the joints.

In order to ensure the stability and convergence of the simulation analysis, numerical simulations considering the pre-stress of the seal ring are carried out. A convergence test of the finite element method and the number of elements is carried out to avoid the problem of non-convergence of the stress results due to stress singularities so that the appropriate mesh density can be determined for subsequent studies. The results of the pre-stress analysis of the inner joint carried out for six different element numbers of seal rings are shown in Figure 6.

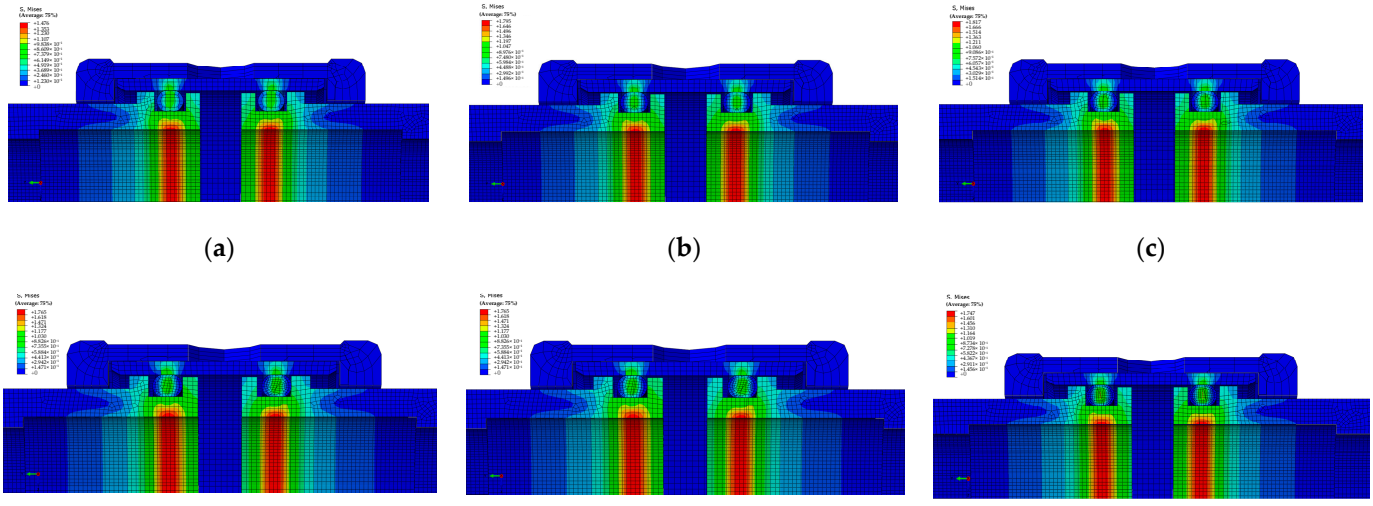

Figure 6. Six different element numbers of seal rings: (**a**) 6272 elements, (**b**) 10,780 elements, (**c**) 14,210 elements, (**d**) 17,885 elements, (**e**) 22,785 elements, (**f**) 36,260 elements.

The effect of different mesh densities on the maximum stress of the inner joints is further analyzed, as shown in Figure 7. The numerical simulation mainly adjusts the mesh density of the seal. From Figure 7, it can be seen that in the range of element numbers [6272, 142,101], the maximum stress fluctuation is larger, and the increase is in the range of 18%. As the grid is encrypted and the number of elements is in a range of [17,885, 36,260], the fluctuation of the maximum stress becomes smaller, and it is kept in the range of 1%. At this point, the maximum stress can be considered to be convergent. The subsequent simulation analysis of the inner joint uses the meshing method shown in Figure 6d with good element quality, and the outer joints use the same method to determine the mesh density.

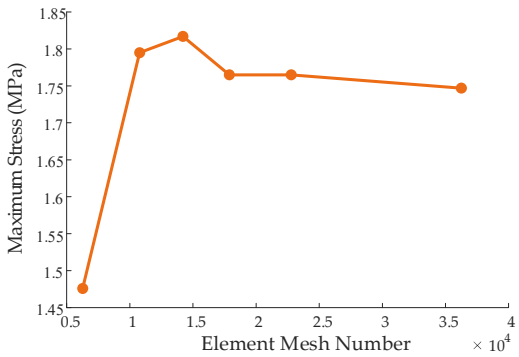

Figure 7. Maximum stress of inner joint under different mesh densities.

Table 1 is drawn to reflect the information on the number of units, number of nodes, etc., determined after the convergence analysis of the inner joint, outer joint, and support block in Figures 8–10, respectively.

Table 1. Number of different component element numbers.

Name	Element Number	Number of Mesh Nodes	Mesh Quality
Outer joint	107,150	143,756	No warning and error
Inner joint	173,050	211,840	No warning and error
Support block	3272	4968	No warning and error

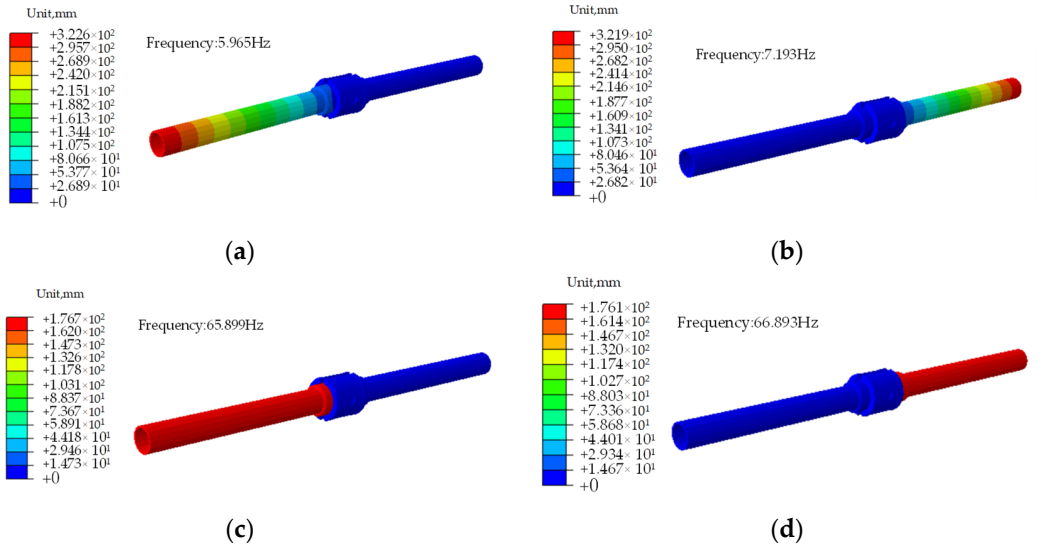

Figure 8. First four orders of pre-stress modes of inner joints. (**a**) First-order pre-stressed mode, (**b**) second-order pre-stressed mode, (**c**) third-order pre-stressed mode, (**d**) fourth-order pre-stressed mode.

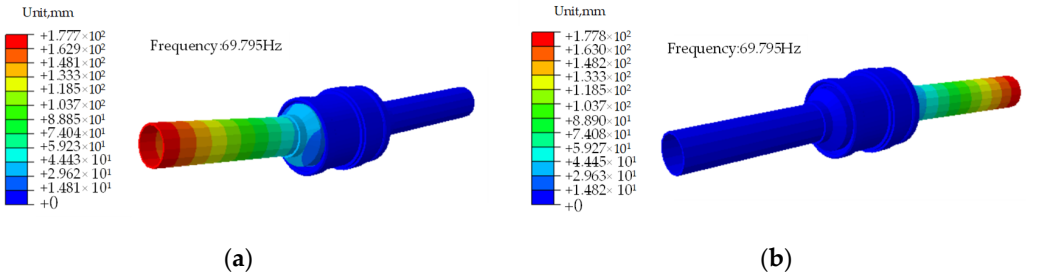

Figure 9. First two orders of pre-stress modes of outer joints. (**a**) First-order pre-stressed mode, (**b**) second-order pre-stressed mode.

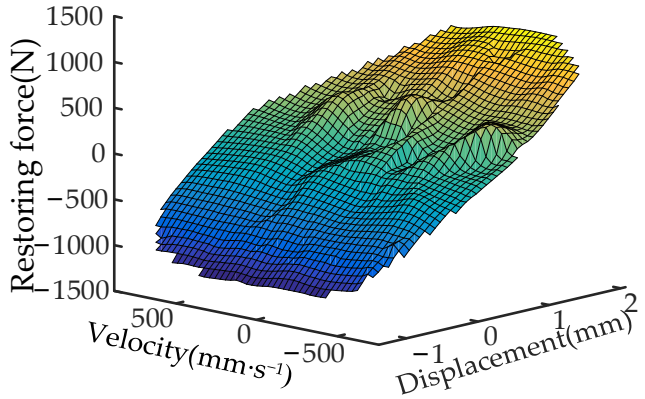

Figure 10. Outer joint sliding motion FSM surface.

The simulation results of constrained modal analysis with pre-stress for the inner and outer joints are shown in Figures 8 and 9.

From Figures 8 and 9, it can be seen that the inner and outer joints have no resonant intrinsic frequency between 10 and 60 Hz. Therefore, the excitation force frequency (torque), f, is taken as three groups of 20 Hz, 30 Hz, and 40 Hz. The friction torque of the sealing ring is generated by the friction between the sealing ring and the mating surface. Under the condition that the metal material and the sealing ring material are determined, the friction force (torque) is mainly determined by the compression of the sealing ring and the roughness of the metal surface [30]. The calculation parameters are shown in Table 2.

Table 2. Sealing ring parameters.

Name	Section Diameter d_1 (mm)	Height after Compression d_2 (mm)	Friction Surface Diameter D (mm)
Outer joint	3.52	2.94	47.304
Inner joint	1.78	1.43	14.757

According to the calculation parameters in Table 2, the friction forces of the inner and outer joints are calculated to be 186.163 N and 40.002 N, respectively, and the friction torques are 4.403 N·m and 0.295 N·m, respectively.

In order to ensure the joint movement, the excitation force (torque) should be greater than the friction force. Through testing, it is found that when the excitation force amplitude of the inner joint is 50 N, the excitation torque amplitude is 0.5 N·m. When the excitation force amplitude of the outer joint is 1000 N, and its excitation torque amplitude is 5 N·m, the inner and outer joints have enough motion.

4.2. Parameter Identification Results of Joint

Since each connection parameter identification process for both the inner and outer joint is identical, we take an example of identifying motion equivalent connection parameters for an outer joint with an excitation frequency of 20 Hz. We also obtain an FSM surface in this case using MATLAB programming, as shown in Figure 10.

From Figure 10, it can be seen that when the speed is 0 mm/s, the relationship between the restoring force and the displacement can be obtained, that is, the equivalent stiffness of the outer joint when the displacement compensation is performed. When the displacement is 0 mm, the relationship between the restoring force and the velocity can be obtained, that is, the equivalent damping of the outer joint when the displacement compensation is performed. The kinematic stiffness and damping curves of the outer joint during displacement compensation are obtained by the section method, as shown in Figures 11 and 12.

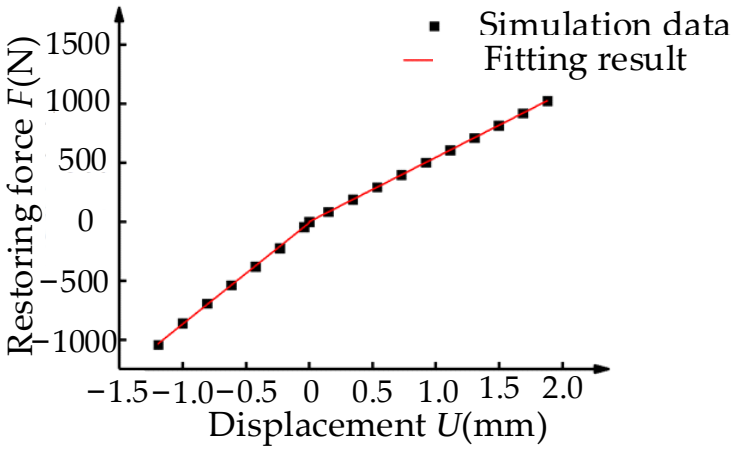

Figure 11. Stiffness curve.

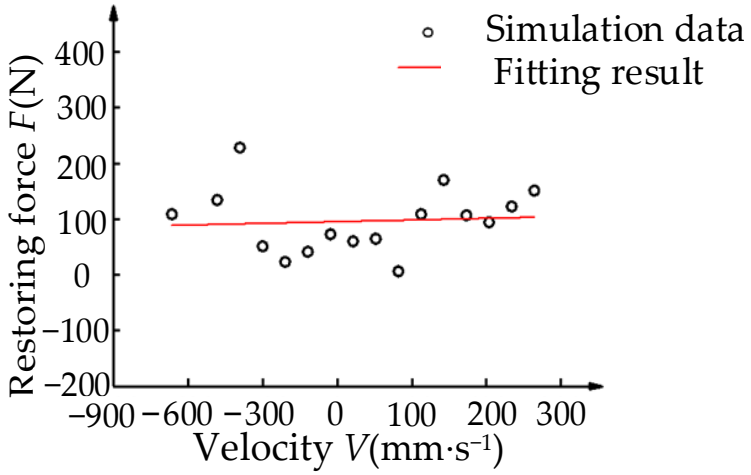

Figure 12. Damping curve.

It can be seen from Figures 11 and 12 that when the outer joint is compensated for displacement, the equivalent stiffness generated by the positive and negative strokes is different and should be fitted separately. The distribution of the damping scatter point is relatively scattered, and the linearization is considered when the specific fitting equation is not determined. Using the least square method to fit the data, it can be obtained that when the outer joint is sliding, the equivalent tensile stiffness of the connection structure is 545.10 N·mm, the equivalent compression stiffness is 858.22 N·mm, and the equivalent damping coefficient is 0.0101 N·mm·s^{-1}.

Similarly, the equivalent connection parameters of the inner and outer joints at all excitation frequencies can be obtained, as shown in Figure 13. The equivalent connection parameters of the sliding, rotational, and torsional motion of the inner and outer joints at each frequency are shown in Tables 3 and 4.

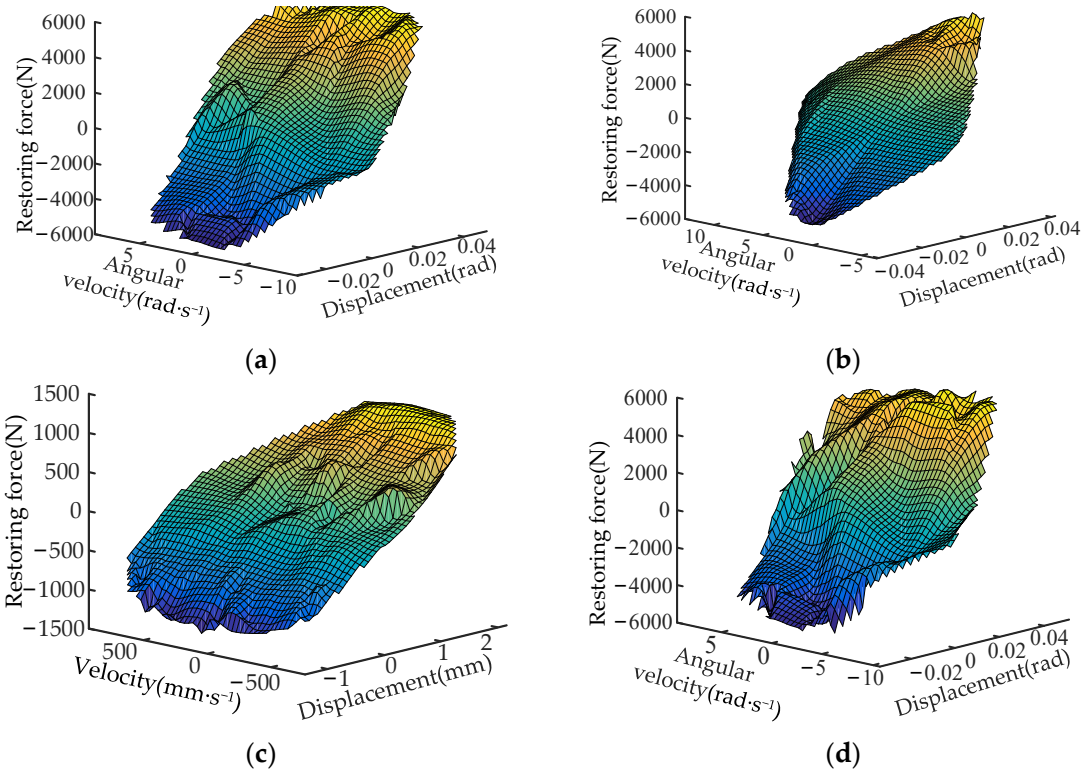

Figure 13. *Cont.*

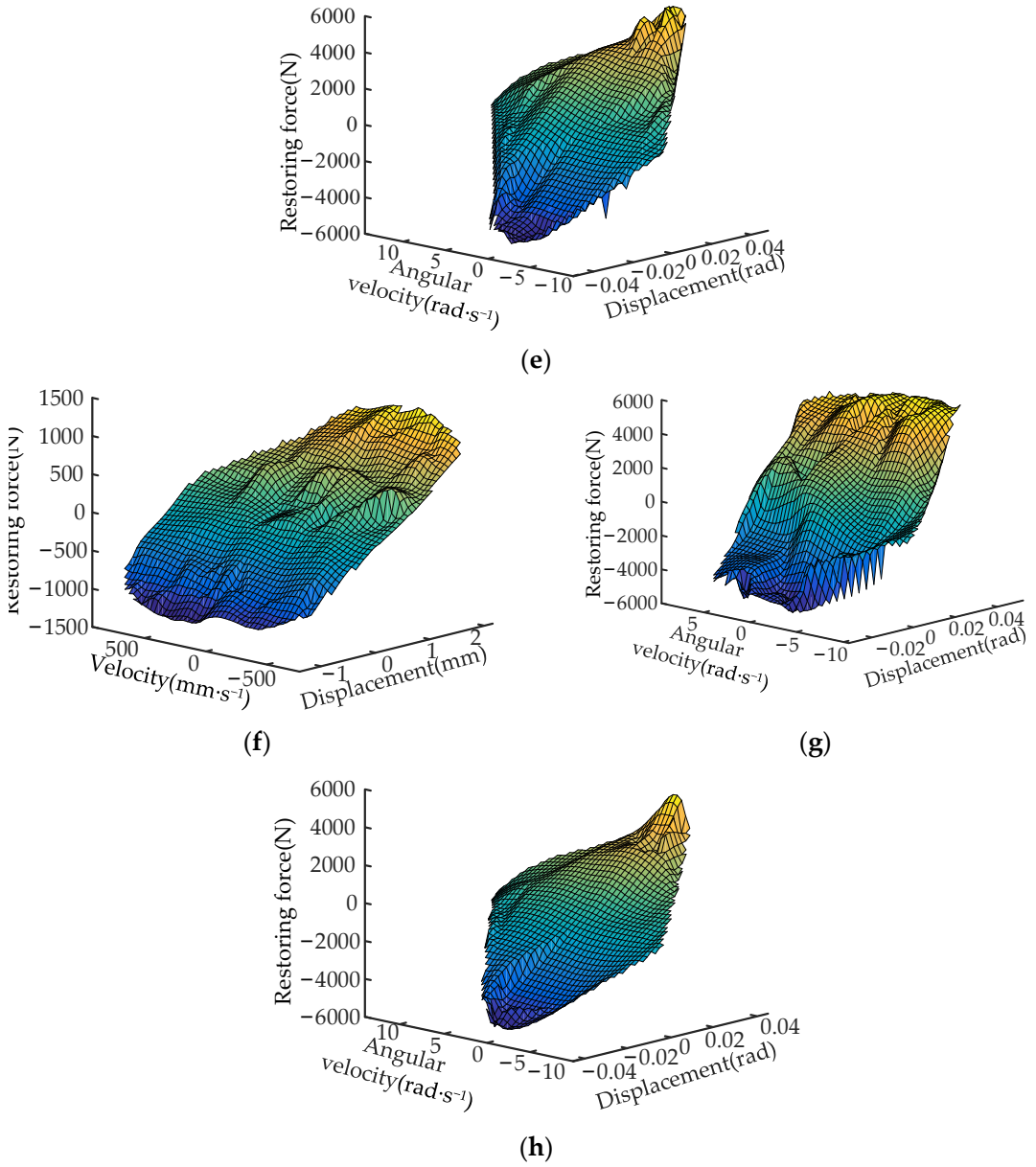

Figure 13. FSM of outer joint: (**a**) 20 Hz rotational motion, (**b**) 20 Hz torsional motion, (**c**) 30 Hz sliding motion, (**d**) 30 Hz rotational motion, (**e**) 30 Hz torsional motion, (**f**) 40 Hz sliding motion, (**g**) 40 Hz rotational motion, (**h**) 40 Hz torsional motion.

Table 3. Equivalent parameters of outer joint under loads with different excitation frequencies.

Frequency (Hz)	Tensile Stiffness (N/mm)	Compressive Stiffness (N/mm)	Slide Damping (N/(mm·s^{-1}))	Rotational Stiffness (N·mm/rad)	Rotational Damping (N·mm/(rad·s^{-1}))	Torsional Rigidity (N·mm/rad)	Torsional Damping (N·mm/(rad·s^{-1}))
20	545.10	858.22	0.0101	146,727.73	13.043	125,595.29	33.07
30	525.45	913.91	0.0177	140,404.97	19.422	111,308.34	28.65
40	551.65	820.28	0.0173	143,151.33	17.316	121,308.36	29.59
Average value	540.73	864.14	0.0150	143,427.84	16.593	119,404.99	30.44

Table 4. Equivalent parameters of inner joint under loads with different excitation frequencies.

Frequency (Hz)	Tensile Stiffness (N/mm)	Compressive Stiffness (N/mm)	Slide Damping ($N/(mm \cdot s^{-1})$)	Rotational Stiffness (N·mm/rad)	Rotational Damping ($N \cdot mm/(rad \cdot s^{-1})$)	Torsional Rigidity (N·mm/rad)	Torsional Damping ($N \cdot mm/(rad \cdot s^{-1})$)
20	38.17	119.48	0.0012	346.75	3.10	888.94	3.08
30	39.32	123.06	0.0014	357.15	3.19	915.61	2.99
40	37.02	115.90	0.0012	336.65	3.01	862.47	3.17
Average value	38.17	119.48	0.0013	346.85	3.10	889.01	3.09

4.3. Parameter Identification Results of Support Block

The equivalent connection parameters of the support block are derived from the linear elastic characteristics of the metal material. According to the FSM surface of the linear system, the equivalent connection parameters can be directly calculated by obtaining the corresponding displacement and velocity under the excitation force.

The outer welding surface of the support block is coupled to one point, and the inner welding surface of the support block is set fixed constraints. Since it has a symmetrical structure, only the positive excitation force along the X-axis and the Y-axis and the clockwise excitation torque around the X-axis and the Y-axis are applied to the coupling point of the support block. The torque is 1 N·mm, and the corresponding displacement and velocity nephograms similar to those are shown in Figure 14.

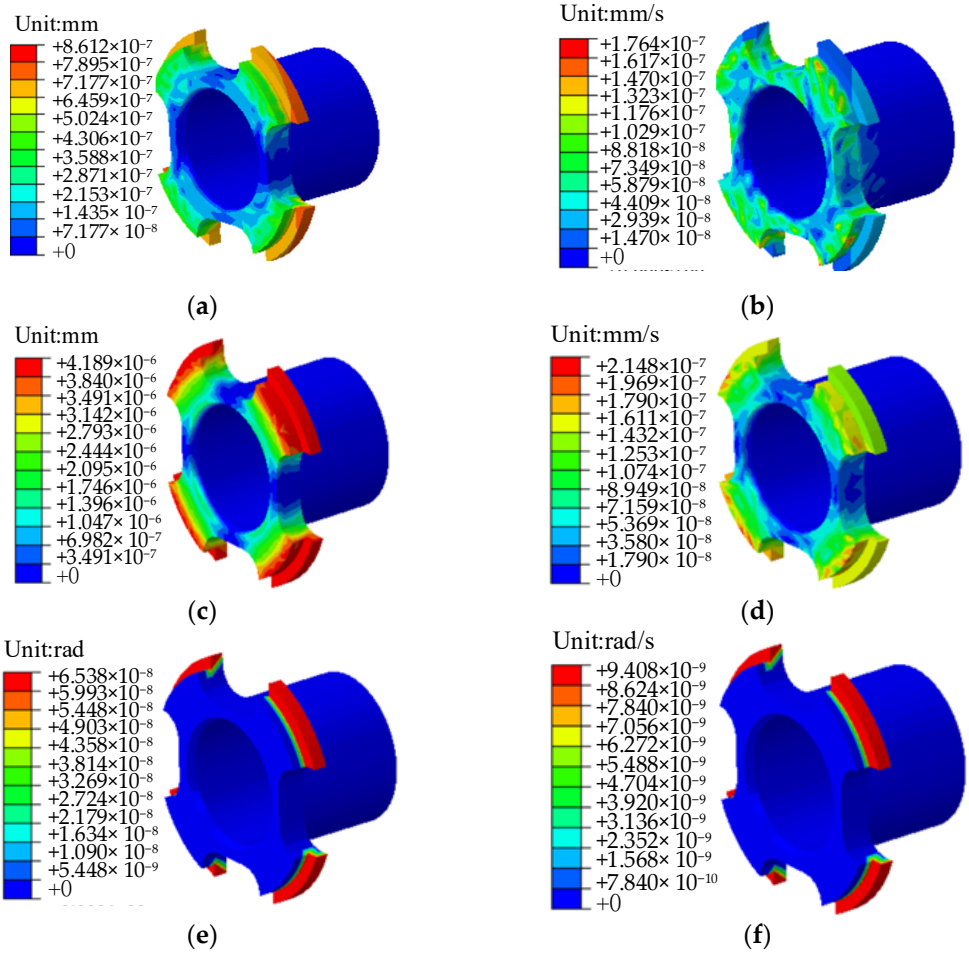

Figure 14. *Cont.*

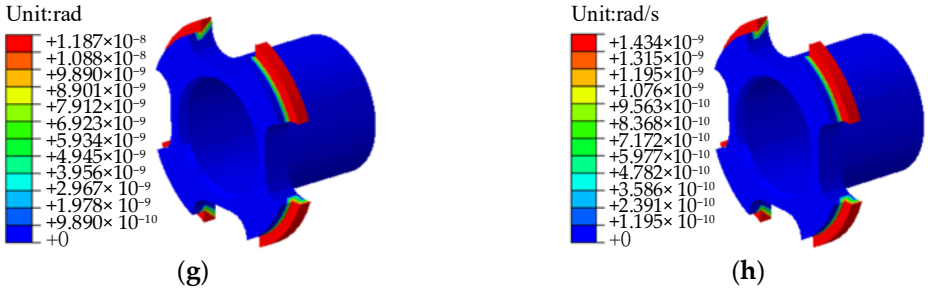

Figure 14. Support block analysis results. (**a**) X-direction displacement, (**b**) X-direction velocity, (**c**) Y-direction displacement, (**d**) Y-direction velocity, (**e**) angular displacement around the X-axis, (**f**) angular velocity around the X-axis, (**g**) angular displacement around the Y-axis, (**h**) angular velocity around the Y-axis.

Thus, the equivalent connection stiffness and damping of the support block are obtained, as shown in Tables 5 and 6.

Table 5. Equivalent connection stiffness of support block.

K_x (N/m)	K_y (N/m)	K_z (N/m)	$K_{\tau x}$ (N·m/rad)	$K_{\tau y}$ (N·m/rad)	$K_{\tau z}$ (N·m/rad)
2.38×10^8	2.38×10^8	2.38×10^8	1.53×10^4	8.42×10^4	1.53×10^4

Table 6. Equivalent connection damping of support block.

C_x (N·s/m)	C_y (N·s/m)	C_z (N·s/m)	$C_{\tau x}$ (N·m·s/rad)	$C_{\tau y}$ (N·m·s/rad)	$C_{\tau z}$ (N·m·s/rad)
4.66×10^9	4.66×10^9	4.66×10^9	1.06×10^5	6.97×10^5	1.06×10^5

5. Free Modal Experiment

5.1. Experimental Method

The test bench is mainly composed of test stands, test systems, sensors, excitation equipment, and general measuring equipment. The principle of the test bench construction is shown in Figure 15.

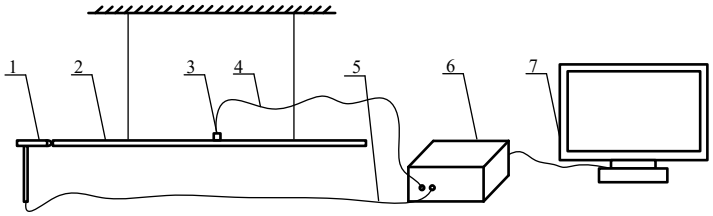

Figure 15. Principle of test bench construction. (1) Force hammer, (2) test pipe, (3) sensor, (4) signal output, (5) signal input, (6) measurement and control system, (7) processor.

The modal experiment generally uses a hammer or the exciter as the excitation device. The experimental object in this paper is the double casing joint, which belongs to light and small equipment. The hammer is used as the excitation equipment, and its specific technical parameters are shown in Figure 16.

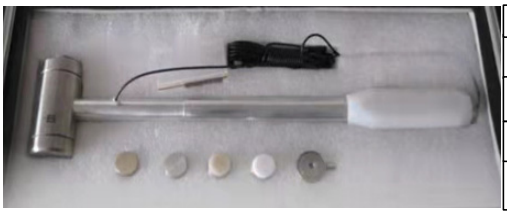

Name	Parameters
Sensitivity(mA/N)	250
Range(N)	0~2000
Operating current(mA)	250mA
Hammer head mass(g)	6

Figure 16. Hammer used in the modal test.

The installation of the test pipe is shown in Figure 17. Acceleration sensors are used to collect vibration response signals and are normally mounted on the surface of the test piece under test using screws and glue. This test uses the acquisition method of mobile excitation points and fixed corresponding points.

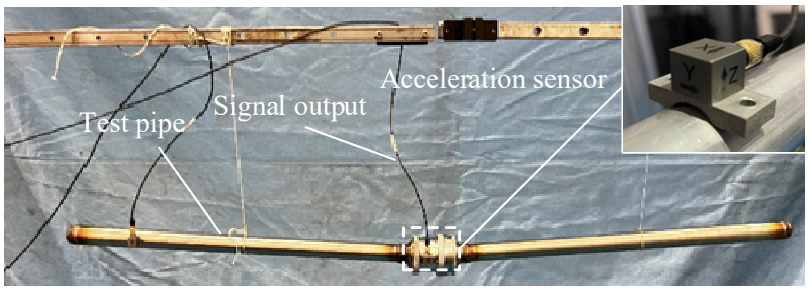

Figure 17. Free modal test installation.

The measurement control system and the data acquisition interface are shown in Figure 18. The test process includes the calibration of test components and the installation of test assemblies. Then, the force hammer is utilized to apply a load to the pipeline unit. The time-domain data acquisition was achieved using an NI measurement control system. Finally, the acquired time-domain signals are transformed into frequency-domain signals by performing fast Fourier transform (FFT) using MATLAB.

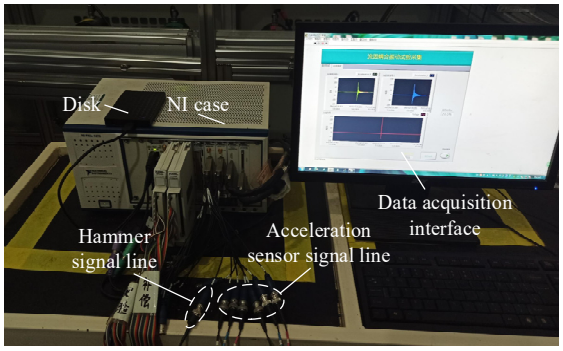

Figure 18. Control system and the data acquisition interface.

5.2. Experimental Result

Figure 19 shows the free modal test results of the double casing joint assembly obtained using the hammering method.

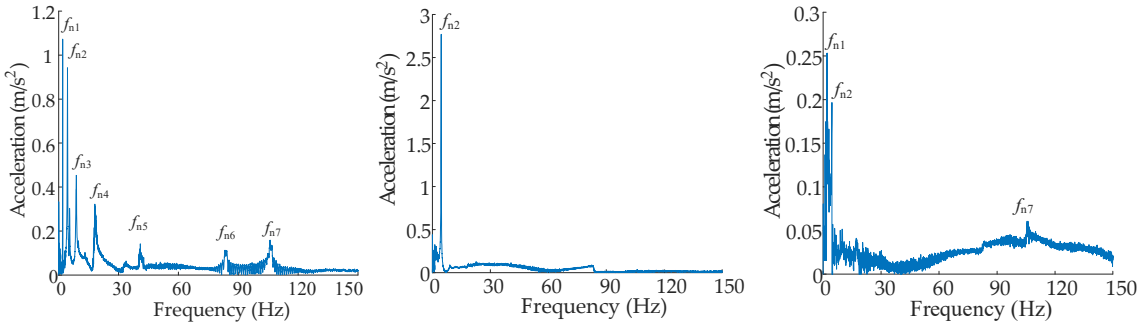

Figure 19. Free modal test results of test pipes. (**a**) X-direction acceleration–frequency response curve, (**b**) Y-direction acceleration–frequency response curve, (**c**) Z-direction acceleration–frequency response curve.

It can be seen from Figure 19 that there are seven main resonance peaks in the range of 0–150 Hz. These seven main resonance peaks appear in the Y-direction, while only the second-order main resonance peaks appear in the X-direction, and the first-order, second-order, and seventh-order main resonance peaks appear in the Z-direction; the natural frequencies of the test component in the free mode are extracted.

6. Numerical Examples

The test assembly dynamics model is established based on the double casing joint dynamics model, and the length of each unit is shown schematically in Figure 20. The geometric and material parameters of the test assembly are shown in Tables 7 and 8.

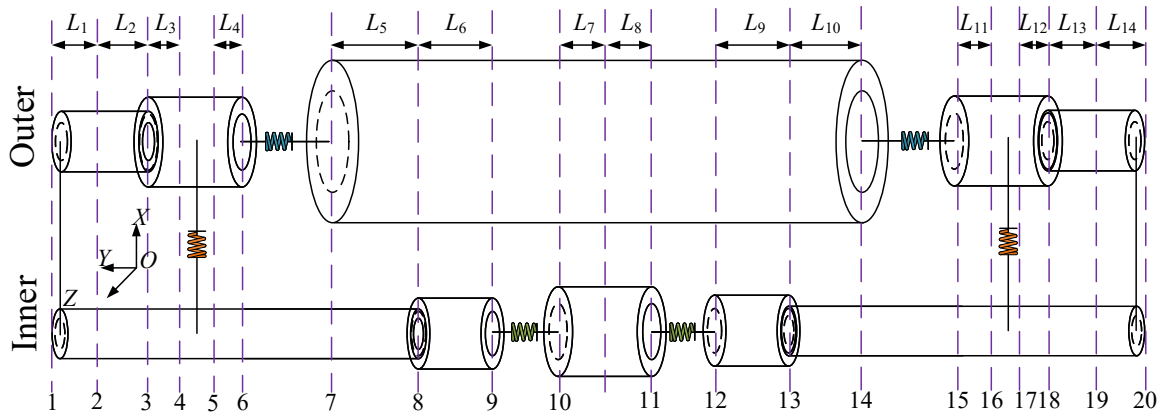

Figure 20. Test component dynamics model cell length.

Table 7. Material parameters of metal parts of double casing joints.

Name	Density (Tone/mm^3)	Elastic Modulus (MPa)	Poisson Ratio
Inner and outer pipes Sleeve Inner and outer socket Support block	7.92×10^{-9}	199,950	0.27
Clamp metal part Bracket	2.73×10^{-9}	73,100	0.33
Nuts and bolts	7.85×10^{-9}	200,000	0.28

Table 8. Remaining geometric and material parameters of the test component.

Material Parameter	Value	Geometric Parameter	Value	Geometric Parameter	Value
Air volume modulus of elasticity (MPa)	0.142	L_1 (mm)	75.38	L_8 (mm)	9.10
Air density (kg/m^3)	1.29	L_2 (mm)	376.87	L_9 (mm)	7.74
Plug quality (kg)	0.003	L_3 (mm)	6.06	L_{10} (mm)	9.88
Sensor quality (kg)	0.006	L_4 (mm)	13.92	L_{11} (mm)	13.92
-	-	L_5 (mm)	9.88	L_{12} (mm)	6.06
-	-	L_6 (mm)	7.74	L_{13} (mm)	376.87
-	-	L_7 (mm)	9.10	L_{14} (mm)	75.38

The sides of the test assembly are free boundary conditions, but the plug mass needs to be taken into account; therefore, the boundary condition matrix of the established dynamic model is expressed as:

$$D = \begin{bmatrix} 1 & 0 & -1 & 0 & 0 & 0 & 0 & 0 & 0 & 0 & 0 & 0 & 0 & 0 \\ 0 & A_f & m_0 s & 1 & 0 & 0 & 0 & 0 & 0 & 0 & 0 & 0 & 0 & 0 \\ 0 & 0 & 0 & 0 & m_0 s & 1 & 0 & 0 & 0 & 0 & 0 & 0 & 0 & 0 \\ 0 & 0 & 0 & 0 & 0 & 0 & 0 & 1 & 0 & 0 & 0 & 0 & 0 & 0 \\ 0 & 0 & 0 & 0 & 0 & 0 & 0 & 0 & m_0 s & 1 & 0 & 0 & 0 & 0 \\ 0 & 0 & 0 & 0 & 0 & 0 & 0 & 0 & 0 & 0 & 0 & 1 & 0 & 0 \\ 0 & 0 & 0 & 0 & 0 & 0 & 0 & 0 & 0 & 0 & 0 & 0 & 0 & 1 \end{bmatrix} \quad (35)$$

The mechanical pulse excitation signal of the hammer at the beginning of the pipe is about 2000 N, and the excitation time is 2 ms. In numerical calculations, the input is in the form of a mechanical pulse excitation, the excitation reversal is negative along the Y-axis, and its corresponding frequency-domain excitation is $(F_r/s)(e^{-sT} - 1)$. Here, Fr is excitation amplitude. When the excitation is in the axial direction of the pipe, the frequency domain–velocity response results of numerical analysis and test can be obtained, as shown in Figure 21.

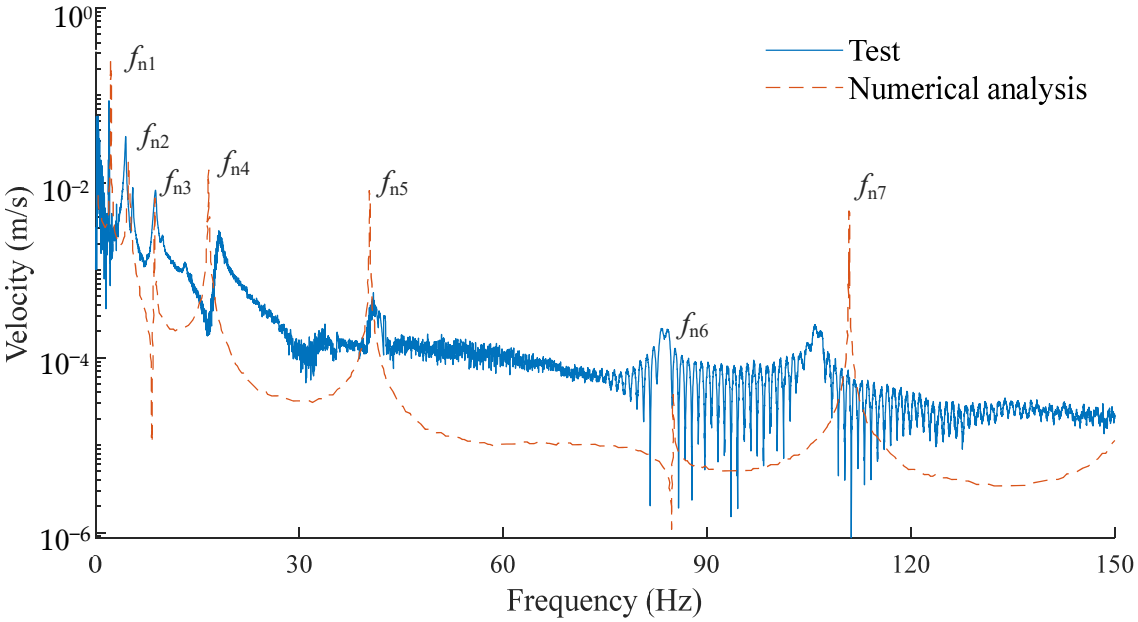

Figure 21. Numerical analysis and experimental frequency domain–velocity response results.

As shown in Figure 21, there are seven main resonance peaks obtained by numerical analysis. The intrinsic frequency values corresponding to each main resonance peak are extracted and compared with the intrinsic frequency values obtained from the modal test, as shown in Table 9.

Table 9. Comparison of test and numerical analysis for each order of intrinsic frequency.

Order	f_{n1}	f_{n2}	f_{n3}	f_{n4}	f_{n5}	f_{n6}
Test (Hz)	1.978	4.527	8.967	18.152	40.910	83.345
Numerical analysis (Hz)	1.791	4.776	9.341	16.923	37.988	80.184
Error	9.45%	5.50%	4.17%	6.77%	7.14%	3.79%

In Table 9, the maximum error under test verification is 9.45%. The main sources of error include the neglect of the outer sleeve reducer structure and the enlarged fluid cross-sectional area of the outer pipe unit. In general, the numerical calculations are consistent with the test results, which verifies the effectiveness of the established dynamic model in dealing with the intrinsic characteristics of casing units containing double casing joints.

7. Conclusions

In this paper, we investigated the dynamic characteristics of an aircraft fuel system pipeline with double casing joints based on the force state and working principle of the inner and outer joints of the double casing joint using a fluid–solid coupling fourteen-equation model and transfer matrices.

Firstly, the fluid–solid coupling dynamics model of the inner and outer joints were established, and the parallel form of the model was adopted. The structural coupling of the inner and outer piping systems was realized, and the analytical solutions were given in the frequency domain. The FSM method was chosen to complete the identification of the connection parameters of the inner and outer joints, which solves the problem of the double casing joint that makes it difficult to measure data by using sensors, as the components are closely combined. Finally, we designed and constructed a double casing joint test bench to test the frequency-domain response under free boundary hammering excitation. The frequency-domain–velocity response under the same excitation was solved by substituting the boundary condition matrix into the established dynamic model.

The accuracy of the theoretical model can be further improved by considering the pipe sleeve reducer structure and experimental studies on the parameter identification in future work.

Author Contributions: Conceptualization, C.G. and L.Q.; methodology, C.F.; software, C.F.; validation, C.F. and L.Q.; formal analysis, C.G.; investigation, C.F.; resources, L.Q.; data curation, R.Y.; writing—original draft preparation, C.F.; writing—review and editing, C.F.; visualization, R.Y.; supervision, C.G. and L.Q.; project administration, C.G. and L.Q.; funding acquisition, L.Q. All authors have read and agreed to the published version of the manuscript.

Funding: This research was funded by the National Natural Science Foundation of China (grant number: 51775477).

Data Availability Statement: The data presented in this study are available on request from the corresponding author.

Acknowledgments: The authors gratefully acknowledge the financial support by the National Natural Science Foundation of China and the testing environment provided by the Hebei Provincial Key Laboratory of Heavy Machinery Fluid Power Transmission and Control. The authors also thank the China Scholarship Council for supporting the two-year research experience of Lingxiao Quan at the RWTH Aachen University and Washington State University.

Conflicts of Interest: The authors declare no conflict of interest.

Nomenclature

Nomenclature of parameters in theoretical and simulation models:

V	Fluid velocity, m/s
P	Fluid pressure, MPa
$\dot{\omega}$	Pipe velocity, m/s
f	Forces in cross-section, N
M	Moment, Nm
x, y, z	Directional subscripts
θ	Deflection angle of pipe, rad
$\dot{\theta}$	Angular velocity of pipe wall, rad/s
m_0	Plug mass, kg

References

1. Wang, C.; Li, Y.G.; Yang, B.Y. Transient performance simulation of aircraft engine integrated with fuel and control systems. *Appl. Therm. Eng.* **2017**, *114*, 1029–1037. [CrossRef]
2. Zhang, Z.; Li, B.; Yu, M.; Liu, Y.; Liu, W. Dynamic strength reliability analysis of an aircraft fuel pipe system. In Proceedings of the 2017 Second International Conference on Reliability Systems Engineering (ICRSE), Milan, Italy, 20–22 December 2017; IEEE: Piscataway, NJ, USA, 2017; pp. 1–6.

3. Novichkov, V.M.; Filinov, N.I.; Kalinina, O.I. Assessment of the Technical Condition of the Aircraft Fuel System by Its Main Elements in Flight. In Proceedings of the 2020 International Multi-Conference on Industrial Engineering and Modern Technologies (FarEastCon), Vladivostok, Russia, 6–9 October 2020; IEEE: Piscataway, NJ, USA, 2020; pp. 1–4.
4. Lamoureux, B.; Massé, J.R.; Mechbal, N. An approach to the health monitoring of a pumping unit in an aircraft engine fuel system. In *PHM Society European Conference*; PHM Society: Rochester, NY, USA, 2012.
5. Wang, Y.; Ruan, C.; Lu, S.; Li, Z. A Study on the Movement Characteristics of Fuel in the Fuel Tank during the Maneuvering Process. *Appl. Sci.* **2023**, *13*, 8636. [CrossRef]
6. Fredricson, H.; Johansen, T.; Klarbring, A.; Petersson, J. Topology optimization of frame structures with flexible joints. *Struct. Multidiscip. Optim.* **2003**, *25*, 199–214. [CrossRef]
7. Melissianos, V.E.; Korakitis, G.P.; Gantes, C.J.; Bouckovalas, G.D. Numerical evaluation of the effectiveness of flexible joints in buried pipelines subjected to strike-slip fault rupture. *Soil Dyn. Earthq. Eng.* **2016**, *90*, 395–410. [CrossRef]
8. Li, X.; Yao, Z.; Yang, M. A novel large thrust-weight ratio V-shaped linear ultrasonic motor with a flexible joint. *Rev. Sci. Instrum.* **2017**, *88*, 65003. [CrossRef]
9. Ettefagh, M.H.; Naraghi, M.; Towhidkhah, F. Position Control of a Flexible Joint via Explicit Model Predictive Control: An Experimental Implementation. *Emerg. Sci. J.* **2019**, *3*, 146–156. [CrossRef]
10. Hongbin, S.; Cai, W.; Zhuanli, Q.; Guocai, L. Numerical Research on Interfacial Damage and Sealing Reliability of Flexible Joint under Wide Temperature Range. *J. Propuls. Technol.* **2019**, *40*, 2313–2324.
11. Song, C.; Du, Q.; Yang, S.; Feng, H.; Pang, H.; Li, C. Flexible joint parameters identification method based on improved tracking differentiator and adaptive differential evolution. *Rev. Sci. Instrum.* **2022**, *93*, 84706. [CrossRef]
12. Xu, X.D.; Li, G.J.; Yuan, S. Application of Flexible Combine-Clamp in Digital Rapid Production for Aircraft Tube. *Appl. Mech. Mater.* **2013**, *404*, 777–781. [CrossRef]
13. Melissianos, V.E.; Lignos, X.A.; Bachas, K.K.; Gantes, C.J. Experimental investigation of pipes with flexible joints under fault rupture. *J. Constr. Steel Res.* **2017**, *128*, 633–648. [CrossRef]
14. Konstantinov, S.V.; Lalabekov, V.I.; Obolenskii, Y.G. Mathematical Model of the Gas-Hydraulic Control Actuator for the Swiveling Nozzle of the Solid Propellant Fuel Propulsion System with Flexible Joint. *Russ. Aeronaut.* **2019**, *62*, 222–228. [CrossRef]
15. Ramezani, M.A.; Yousefi, S.; Fouladi, N. An experimental and numerical investigation of the effect of geometric parameters on the flexible joint nonlinear behavior for thrust vector control. *Proc. Inst. Mech. Eng. Part G J. Aerosp. Eng.* **2019**, *233*, 2772–2782. [CrossRef]
16. Li, L.; Xu, W.; Tan, Y.; Yang, Y.; Yang, J.; Tan, D. Fluid-induced vibration evolution mechanism of multiphase free sink vortex and the multi-source vibration sensing method. *Mech. Syst. Signal Process.* **2023**, *189*, 110058. [CrossRef]
17. Li, L.; Lu, B.; Xu, W.X.; Gu, Z.H.; Yang, Y.S.; Tan, D.P. Mechanism of multiphase coupling transport evolution of free sink vortex. *Acta Phys. Sin.* **2023**, *72*, 34702. [CrossRef]
18. Zhang, X.M. Parametric studies of coupled vibration of cylindrical pipes conveying fluid with the wave propagation approach. *Comput. Struct.* **2002**, *80*, 287–295. [CrossRef]
19. Xu, Y.; Johnston, D.N.; Jiao, Z.; Plummer, A.R. Frequency modelling and solution of fluid-structure interaction in complex pipelines. *J. Sound Vib.* **2014**, *333*, 2800–2822. [CrossRef]
20. Selvarajan, S.; Tappe, A.A.; Heiduk, C.; Scholl, S.; Schenkendorf, R. Process Model Inversion in the Data-Driven Engineering Context for Improved Parameter Sensitivities. *Processes* **2022**, *10*, 1764. [CrossRef]
21. Jin, H.; Liu, Z.; Zhang, H.; Liu, Y.; Zhao, J. A Dynamic Parameter Identification Method for Flexible Joints Based on Adaptive Control. *IEEE/ASME Trans. Mechatron.* **2018**, *23*, 2896–2908. [CrossRef]
22. Asarin, E.; Donzé, A.; Maler, O.; Nickovic, D. Parametric Identification of Temporal Properties. In Proceedings of the Runtime Verification: Second International Conference, RV 2011, San Francisco, CA, USA, 27–30 September 2011; Springer: Berlin/Heidelberg, Germany, 2012; Volume 7186, pp. 147–160.
23. Al-Hadid, M.A.; Wright, J.R. Estimation of mass and modal mass in the identification of non-linear single and multi degree of freedom systems using the force-state mapping approach. *Mech. Syst. Signal Process.* **1992**, *6*, 383–401. [CrossRef]
24. Kimm, W.; Park, Y. Non-linear joint parameter identification by applying the force-state mapping technique in the frequency domain. *Mech. Syst. Signal Process.* **1994**, *8*, 519–529. [CrossRef]
25. Wang, J.; Huang, H. Model and parameters identification of non-linear joint by force-state mapping in frequency domain. *J. Mech.* **2007**, *23*, 367–380. [CrossRef]
26. Shu, Y.; Liu, Y.; Xu, Z.; Zhao, X.; Chen, M. Optimization of Hydraulic Fine Blanking Press Control System Based on System Identification. *Processes* **2023**, *11*, 59. [CrossRef]
27. Gao, H.; Guo, C.; Quan, L.; Wang, S. Frequency Domain Analysis of Fluid–Structure Interaction in Aircraft Hydraulic Pipe with Complex Constraints. *Processes* **2022**, *10*, 1161. [CrossRef]
28. Quan, L.; Luo, H.; Zhang, J. Harmonic Response Analysis of Axial Plunger Pump Shell Structure. *Chin. Hydraul. Pneum.* **2014**, *5*, 33–39.

29. Chen, Y.; An, C.; Zhang, R.; Fu, Q.; Zhu, R. Research on Two-Way Contra-Rotating Axial-Flow Pump–Turbine with Various Blade Angles in Pump Mode. *Processes* **2023**, *11*, 1552. [CrossRef]
30. Jalali, H.; Ahmadian, H.; Mottershead, J.E. Identification of nonlinear bolted lap-joint parameters by force-state mapping. *Int. J. Solids Struct.* **2007**, *44*, 8087–8105. [CrossRef]